All-Optical Mode-Selective Router Based on Broken Anti-$\mathcal{PT}$ Symmetry

Feifan Wang,[1] Xinxiang Niu,[1] Xiaoyong Hu,[1,2,3,*] Tingyi Gu,[4,†] Xingyuan Wang,[5,‡] Jinghuan Yang,[1] Hong Yang,[1,2,3] Yutian Ao,[1] Shufang Wang,[6] and Qihuang Gong[1,2,3]

[1] *State Key Laboratory for Mesoscopic Physics, Department of Physics, Collaborative Innovation Center of Quantum Matter, and Frontiers Science Center for Nano-optoelectronics, Beijing Academy of Quantum Information Sciences, Peking University, Beijing 100871, People's Republic of China*

[2] *Peking University Yangtze Delta Institute of Optoelectronics, Nantong, Jiangsu 226010, People's Republic of China*

[3] *Collaborative Innovation Center of Extreme Optics, Shanxi University, Taiyuan, Shanxi 030006, People's Republic of China*

[4] *Electrical and Computer Engineering, University of Delaware, Newark, Delaware 19711, USA*

[5] *College of Mathematics and Physics, Beijing University of Chemical Technology, Beijing 100029, China*

[6] *College of Physics Science and Technology, Hebei University, Baoding, Hebei 071002, China*

(Received 3 June 2020; revised 24 August 2020; accepted 21 September 2020; published 27 October 2020)

On-chip integration fundamentally changes the way in which information is processed. The exploding communication capacity requires a high degree of integration of optical devices in a limited footprint. These requirements have pushed the minimization of optical chips almost to their physical limits. One potential way to break this limitation is to increase the number of functionalities in a module, for which the most critical issue is to expand the degree of freedom of information processing. Here, we propose a degree of freedom of information processing based on the basic mode vectors in the anti-parity-time-symmetry system. Based on our principle, adjacent whispering-gallery modes in a ring cavity are remarkably distinguished in their sensitivity to the signal intensity. What is more, the desired modes are labeled by individual resonance frequencies. This principle is demonstrated experimentally based on the wavelength-selective nonlinear excitation in microring resonators with the nonlinear material Bi_2Se_3. In addition, the combination of this proposed degree of freedom and the signal-direction-dependent function is experimentally demonstrated. This research provides a degree of freedom for designing multifunction devices, which will fundamentally expand the capacity of on-chip information processing.

DOI: 10.1103/PhysRevApplied.14.044050

I. INTRODUCTION

Integrated photonics, which shows excellent performance with regard to speed, bandwidth, and stability, is one of the most promising successors of integrated electronics [1–4]. However, the growing demand for expanding information-processing capabilities on chip has pushed the minimization of optical devices almost to its physical limit, such as the size limit resulting from the diffraction limit of photons and the tunneling effect [5–10]. To break this limitation, it is helpful to expand the degrees of freedom in information processing. The utilization of more degrees of freedom means encoding more information in the input of a device and then more functions can be realized on chip by processing the input. The conventional degrees of freedom for designing optical devices include wavelengths [11,12], polarizations [13,14], and intensities [15,16]. One degree of freedom must be tunable after passing specific optical structures or being stimulated by external signals in order to carry information. Therefore, there has been little progress in the exploration of degrees of freedom. Here, we propose a degree of freedom in information processing based on the basic mode vectors in the system that exhibits anti-parity-time ($\mathcal{PT}$) symmetry. The nonlinear responses of adjacent whispering-gallery modes in a microring are distinguished on the basis of our principle.

Optical $\mathcal{PT}$-symmetric systems have been well studied for their potential in controlling mode profiles. The $\mathcal{PT}$ symmetry (or anti-$\mathcal{PT}$ symmetry) of an optical system is determined by the distribution of the refractive index in the system. In optical $\mathcal{PT}$-symmetric systems, the real parts of the refractive index are symmetric about a spatially symmetric axis and the imaginary parts are antisymmetric. When the $\mathcal{PT}$-symmetric structure is excited at the designed wavelength, a spontaneous symmetry

*xiaoyonghu@pku.edu.cn
†tingyigu@udel.edu
‡wang_xingyuan@mail.buct.edu.cn

breaking modifies longitudinal mode profile according to the nonuniform refractive index profile. These modes satisfying the $\mathcal{PT}$-symmetry-breaking criteria can strongly enhance light-matter interactions in specific regions [17–22]. However, in a $\mathcal{PT}$-symmetry system, the imaginary parts of the eigenfrequencies diverge, while their real parts are still degenerate at the $\mathcal{PT}$ broken phase [23–26]. This means that the loss and/or gain of the modes differs, while the resonant frequencies of the modes are still the same. As $\mathcal{PT}$ symmetry focuses on nondegenerate imaginary parts of the eigenfrequency, we explore an anti-$\mathcal{PT}$ symmetry with a controllable nondegenerate real part of their eigenfrequencies. In a microring-resonator-based mode-selective all-optical switch, a subwavelength periodic cladding with a higher real refractive index is added by following the principles of the anti-$\mathcal{PT}$-symmetry concept [27,28]. Within a pair of eigenmodes, one mode has a much better overlap coefficient with the cladding material. The orders-of-magnitude-higher optical nonlinearity of the cladding material, compared to silicon, leads to more efficient optical-tuning efficiency of this mode. In this way, by breaking the anti-$\mathcal{PT}$ symmetry, we realize different nonlinearities in two adjacent resonances. This design significantly increases the signal-processing capacity (for a detailed comparison, see the Supplemental Material [29]).

II. MODE-SELECTIVE NONLINEAR COEFFICIENT IN BROKEN ANTI-$\mathcal{PT}$ SYMMETRY

Here, we design a 34-order periodical structure with interleaving bare Si and hybrid Bi_2Se_3-on-Si areas [Fig. 1(a)]. As a member of the topological insulators, Bi_2Se_3 has been explored for its typical band structures [30] and has also shown its outstanding electrical [31] and optical nonlinear [32] performances. However, there has been little work about Bi_2Se_3-based optical logic devices. In this work, Bi_2Se_3 is enrolled into the system for its optical nonlinearity and its potential in future opto-electronic integration. A 50-nm-thick Bi_2Se_3 film is deposited on a microring resonator by the pulsed-laser-deposition (PLD) method. After lithography and etching,

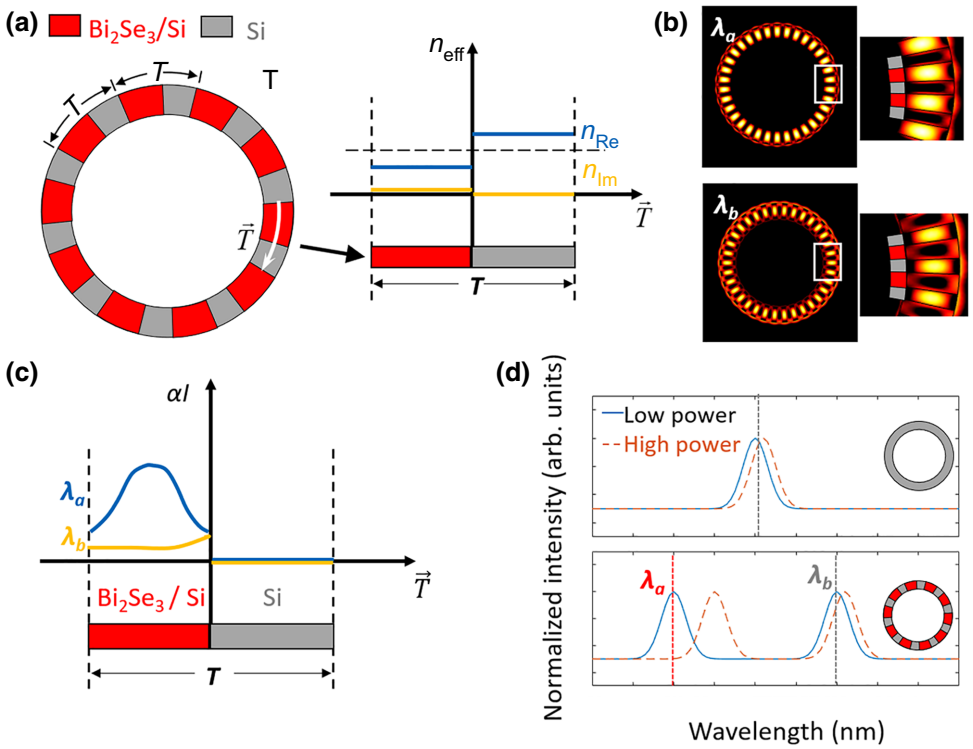

FIG. 1. (a) The top view of the microring resonator periodically patterned by Bi_2Se_3 with spatial period T. The variation of the effective complex refractive index is shown as the right inset. (b) The electric field intensity distributions of modes at $m = 34$ in the hybrid ring. For the mode around 1480 nm (upper) and 1560 nm (lower), the fields are confined in the Bi_2Se_3/Si hybrid area and the bare-silicon area, respectively. Therefore, the nonlinearity of the mode around 1480 nm is much higher. (c) The product of the absorption coefficient α and the light intensity I in one period. At λ_a, there is remarkable absorption in Bi_2Se_3/Si. At λ_b, as most of the field is in silicon, which has a low absorption coefficient, there is no remarkable value of αI in the whole period. (d) The eigenmodes inside a ring resonator. Upper: in a pure-silicon ring, the nonlinear effect is weak. Lower: with the scattering structure, the resonance splits into two peaks. The two new modes suffer a spontaneous symmetry breaking as in (b). When the signal inside the ring is strong enough, both peaks will shift but the shifts are at a different scale.

55% of the waveguide is covered by Bi_2Se_3. The effective index of the waveguide varies periodically from between 2.46 and (2.07+0.05i). In optics, the anti-$\mathcal{PT}$-symmetric Hamiltonian requires that the real and imaginary parts of the refractive distribution must be odd and even functions, respectively [22]. The refractive-index profile on the perimeter of the microring follows anti-$\mathcal{PT}$ symmetry with respect to the boundary between the regions with and without Bi_2Se_3. The horizontal black dashed line in the right-hand image in Fig. 1(a) denotes the reference value for evaluating the change of the real part of the refractive index. It is noted that although bulk Bi_2Se_3 is very lossy, the imaginary part of the effective refractive index here is not large. The reason lies in the short length of the period. Between the two kinds of regions, the mode slowly converts. As the period is short enough, even in the region with Bi_2Se_3 cladding, the mode remains similar to that in the pure-silicon region. The electric field is still mostly distributed in the silicon part [29].

In this system, clockwise (counterclockwise) traveling waves get scattered at the slices and the constructive (destructive) interference of the clockwise (counterclockwise) modes makes standing waves. This is the origin of the standing eigenmodes of the cavity [33]. The two 34-azimuthal-order resonant modes in the ring suffer a spontaneous symmetry breaking [34] and their field distributions are different. Our simulation results [Fig. 1(b)] verify the disparate field distributions of the two 34-azimuthal-order modes. The field is mostly confined within the regions with Bi_2Se_3 tops for the mode at about 1480 nm (λ_a), while for the mode at 1560 nm (λ_b), the regions of bare silicon are brighter. The in-plane mode overlap factor with the hybrid area is 0.45 at λ_a and 0.8 at λ_b. The design of the refractive-index profile follows the principle of anti-$\mathcal{PT}$ symmetry, which results in the largest degree of mode splitting [29].

Several previous works have taken advantage of this field-intensity nonuniformity in $\mathcal{PT}$-symmetry breaking to construct a mode difference. Mode-selective gain through periodic patterning has been widely used in lasers [17,18,34]. In those works, modes with a higher optical overlap coefficient with gain materials are selectively enhanced and thus the threshold for lasing is reduced. Here, we apply some similar design concepts with a different physical concept and focus on the enhancement of nonlinear effects. Although some details of the design look similar, to distinguish the optical signals, we explore an anti-$\mathcal{PT}$-symmetric system to obtain a controllable nondegenerate real part of their eigenfrequencies. Compared to $\mathcal{PT}$-symmetric systems in previous works, anti-$\mathcal{PT}$ systems make it easier to distinguish the eigenmodes by wavelength. Besides, instead of just inducing gain or loss into the eigenmodes, we focus on the modulation of optical nonlinearities by using the field-intensity nonuniformity. A remarkable difference between the thermal-optic shifts of the eigenmodes is realized, leading to a better modulation of the signals. Given the continuous laser excitation, thermal optic nonlinear effects dominate the refractive-index shift. In microrings, the shift of the resonance wavelength $\Delta\lambda$ is determined by

$$\Delta\lambda = \Delta n/n \times \lambda, \tag{1}$$

where Δn is the change in the local refractive index and λ is the original resonance wavelength. In our case, $\lambda_a - \lambda_b \ll \lambda_a$ (or λ_b), so the shift mostly depends on Δn. In thermal-optic nonlinear effects, Δn can be described as $\Delta n = dn/dT \times \Delta T$, where dn/dT is the effective refractive-index change per degree of temperature increase and ΔT is the incremental temperature. The distribution of dn/dT only depends on the material distribution and shows hardly any difference between λ_a and λ_b. However, the ΔT values of the two resonances are different. According to previous works [35,36], ΔT should be quite uniform along the perimeter of the ring, as the thermal-diffusion length (tens of micrometers in SOI) is much longer than the spatial period T and is proportional to the total linear absorption:

$$\int_0^T \alpha I dL = \int_0^{0.55T} \alpha_{\text{Bi-Se-Si}} I_{\text{Bi-Se-Si}} dL + \int_{0.55T}^{T} \alpha_{\text{Si}} I_{\text{Si}} dL, \tag{2}$$

where $\alpha_{\text{Bi-Se-Si}}$ and α_{Si} are the absorption coefficients in the hybrid and monolithic regions, respectively [marked as yellow lines in the inset of Fig. 1(a)]. $I_{\text{Bi-Se-Si}}$ and I_{Si} are the spatially dependent light intensities in the hybrid and monolithic regions, respectively [Fig. 1(b)]. Both the absorption and the intensity vary periodically along the perimeter (dL). As $\alpha_{\text{Bi-Se-Si}}$ is much larger than α_{Si}, the optical resonance with a higher $I_{\text{Bi-Se-Si}}$ [λ_a in Fig. 1(b)] exhibits a larger refractive-index change, and thus a larger resonance-wavelength shift, than the other resonance mode [λ_b in Fig. 1(b)]. As shown in Fig. 1(c), the total average αI for λ_a is higher than λ_b. Therefore, the nonlinear shift of the resonance at λ_a is larger, as shown in the schematic in Fig. 1(d).

III. MODE-SELECTIVE ALL-OPTICAL SWITCH

As an optical switch, the resonance wavelength of the ring resonator can be controlled by optical, thermal, or electrical stimuli [37,38] and all the resonances are shifted simultaneously. By introducing the anti-$\mathcal{PT}$-symmetry structure on the microring, the nonlinearity becomes mode selective, resulting in different working functions at two different wavelengths (λ_a and λ_b) in our device.

Figure 2 shows the simulated and experimental results of the mode-selective switch. A patterned microring resonator is side coupled to two waveguides that connect to through and drop ports, respectively. The input and output

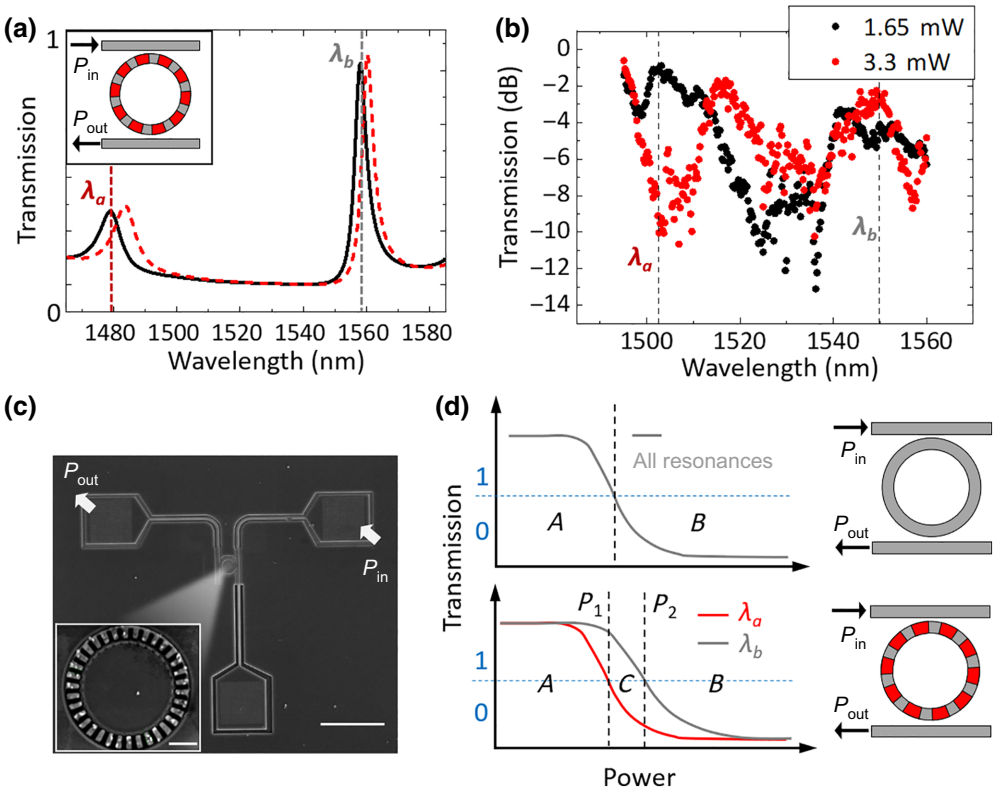

FIG. 2. (a) Simulated transmission spectra at low (black solid curve) and high (red dashed curve) power input. The inset shows the working function of the mode-selective nonlinear switch. (b) Measurement results corresponding to (a). (c) A scanning-electron-microscope (SEM) image of the fabricated add-drop resonator as a switch: scale bar 20 μm. The inset shows details on the ring: scale bar 1 μm. (d) The power-dependent transmission for an unpatterned (upper) and a patterned resonator structure (lower) in Fig. 1. The dashed lines mark the threshold between the "0" and "1" states.

ports of the transmission spectra are marked with black arrows in the inset of Fig. 2(a). Assuming that a continuous wave is launched into the waveguide from the upper left (input) port, the light can couple into the lower left (drop) port through the ring, if the wavelength of the input light overlaps with the resonance [λ_a and λ_b in Fig. 2(a)]. As mentioned in the previous section, by breaking the anti-$\mathcal{PT}$ symmetry of the system, we realize the shift of one specific mode: the mode around λ_a is tuned by changing the signal intensity, while the other resonance around λ_b does not shift as much. Figure 2(a) shows the simulated transmission spectra of the add-drop resonator, which shows this difference in the peak shift. The solid black line shows the transmission at a lower intensity, when the nonlinearities can be neglected, while the red dashed line is the transmission at a higher intensity, when the resonances are red shifted owing to nonlinear effects. Comparing the two curves, we see that the resonance peak around λ_a has a larger shift compared to the peak around λ_b.

Under a nonlinear shift, the original on-resonance wavelength λ_a becomes off resonance and the signal at λ_a would get to the upper left port instead of the lower left one. In this way, the transmission of the signal light at λ_a can be switched [28]. As for λ_b, which has a much smaller nonlinear response, the route of the signal remains relatively stable when the signal intensity varies. Therefore, we can switch the transmission of λ_a while keeping λ_b almost undisturbed. In this way, the device works as a mode-selective switch.

The measured transmission spectra of the signals are shown in Fig. 2(b), with the input and output ports of the transmission spectra marked with white arrows in the SEM image of the device [Fig. 2(c)]. In the experiment, the Bi_2Se_3 film is grown on a commercial silicon-on-isolator substrate by PLD, using a Xe-Cl laser ($\lambda = 308$ nm). The patterns are then fabricated by focused ion-beam deposition (FEI Helios Nanolab 600i). The black dots are the data for a relatively weak signal, while the red dots denote the spectrum of a stronger signal. Here, the peaks are slightly different from the simulation result due to some random errors during fabrication. The widths of the slices may not be equal, which leads to a shift in the resonance position. However, we can still observe the difference in the shifts of the two peaks. From the distance between the red dots and the black dots, it is obvious how the output intensity changes according to the input intensity at λ_a and λ_b. Here, the on:off ratio of this prototype is around 8 dB, which can be further optimized in future work. The relatively low signal contrast here is mostly due to the scattering loss from the patterns on the microring resonator. Better performance can be realized by some optimization of the techniques, for example, by mixing the nonlinear materials with the silicon instead of depositing the top slices. The thickness of the Bi_2Se_3 film is also optimized for the trade-off between the loss and nonlinear effects.

This mode-selective nonlinear behavior makes it possible to obtain an additional logic state in the cavity. In monolithic silicon devices, the relations between the

transmittance and the signal power of all the resonances are indistinguishable. As shown in Fig. 2(d), there are only two states in the ring, *A* ("11") and *B* ("00"), at the through port of the add-drop cavity. The reason is that all the resonances are sharing almost the same nonlinearity of the silicon waveguide. However, in our design, the transmittance of λ_b changes much more slowly than that of λ_a owing to the different nonlinearities for the two modes. There is a state *C* ("01") in which the transmittances of the two wavelengths are different. This additional state makes it much easier to integrate more functions into a system.

IV. MODE-SELECTIVE ROUTER

The mode-selective switch has some potential for integrated multifunctional systems. Combining the mode-selective switch and other optical components such as photonic crystals, we demonstrate a mode-selective router (Fig. 3). The photonic crystal heterojunctions serve as optical insulators within the working wavelength [29,38,39]. The heterojunctions are placed on the two ports of the ring [Fig. 3(a)] to control the direction of photon flow.

The schematics and a SEM image of the device are shown in Figs. 3(a) and 3(b), respectively. Figure 3(c) shows the working function of this module. To explain the origin of this working function, we need to analyze the influences of both the ring and the photonic crystals. For λ_a:

(1) When the signal goes into the system from port *A*, the route of the light is determined by the signal intensity. For a weaker signal, the light couples with the ring and goes out from port *B*. For a stronger signal, the light becomes off resonance owing to the resonance shift and the signal is emitted from port *D*.

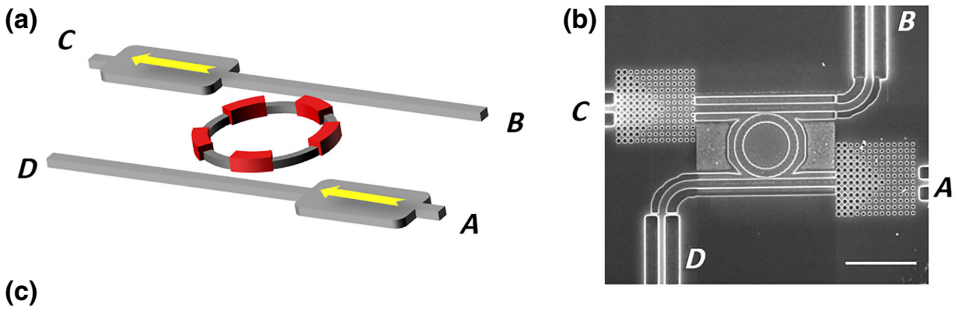

FIG. 3. (a) The schematics of the on-chip router and (b) a SEM image of the fabricated device. Scale bar 5 μm. (c) The designed and (d) measured function tables of the router. The data in black are the transmission when the input power is low (1.65 mW), while the data in red are when the input power is relatively higher (3.3 mW).

(c)

Power Low/High	Output *A*	*B*	*C*	*D*
Input *A*	x	λ_a, λ_b/λ_b	x	x/λ_a
B	x	x	λ_a, λ_b	x
C	x	x	x	x
D	x	x	λ_a , λ_b	x

(d)

Power Low/High	Output *A*	*B*	*C*	*D*
Input *A*	x	T_a = −5.47 dB, T_b = −3.00 dB /T_a = −6.02 dB, T_b = −3.73 dB	x	T_a = −11.02 dB, T_b = −9.71 dB /T_a = −3.88, T_b = −5.70 dB
Input *B*	<-10 dB	x	T_a = −8.16 dB, T_b = −5.72 dBdB /T_a = −7.88 dB, T_b = −7.75 dB	x
Input *C*	x	<-10 dB	x	<-10 dB
Input *D*	<-10 dB	x	T_a = −6.99 dB, T_b = −5.25 dB /T_a = −6.46 dB, T_b = −4.35 dB	x

(2) When a signal at λ_a enters the system from either *B* or *D*, as there is no photonic crystal scattering the light, the signal would be stronger than that from *A* and the peak is slightly red shifted. Therefore, λ_a is no longer just at the peak. As only part of the power is coupled to the ring, the signal can partially get to port *C*. Another part of the power gets to port *A* but cannot pass the photonic crystal. Therefore, there is only output from port *C*. When the signal is stronger, the peak is shifted but the shift is larger than the distance to the dip, so part of the energy can still get to port *C*.

(3) When the signal enters the system from port *C*, the signal is blocked.

For λ_b, the nonlinear response is much lower, so it shares the same routing with a low-power signal at λ_a. Thus, the routing for λ_a is as shown in the table. The contrast ratio of the different ports of this module is around 5 or 6 dB and further optimization on the heterojunction structure, and also the microring, in our future work should be helpful with regard to its performance.

It is possible to obtain the functions of several different devices from this system. For example, when there are two signals going into both port *B* and port *D*, the signal can be regarded as one signal of 3.3 mW and the signal still emerges from port *C*. From above, we can conclude that the device works as an OR gate [40]. These derived functions will be helpful for on-chip integrated circuits [41,42].

Then, we characterize the multiport device in a fiber-coupling system (for details of the fabrication and measurement methods, see Sec. 5 of the Supplemental Material [29]). The transmission of different routes at λ_a and λ_b is summarized in Fig. 3(d). The transmission fits well with the design in Fig. 3(c). For example, when the power is low and is injected into port *A* at λ_a, the transmission to port *B* is higher than that to port *D*. Therefore, we can conclude that when a weak signal at λ_a is injected into port *A*, most of the energy will emerge from port *B*. Other data can be analyzed in a similar way.

More detailed data sets are presented in Fig. 4. The solid circles mark the output intensities at a lower input power at wavelength λ_a and λ_b, while the hollow circles mark the output intensities at a higher input power. The signal intensities when the light enters into the system from ports *A*, *B*, *C*, and *D* are measured and shown in Figures 4(a)–4(d), respectively. As the transmission spectra of the photonic crystal heterojunction are very flat, the line shape of the spectra is determined by the features of an add-drop microring cavity. These curves can be divided into three groups, as follows:

(1) For *A*-*B* in (a) and *D*-*C* in (c), the signal light goes to the output after coupling with the ring, so the curve shows

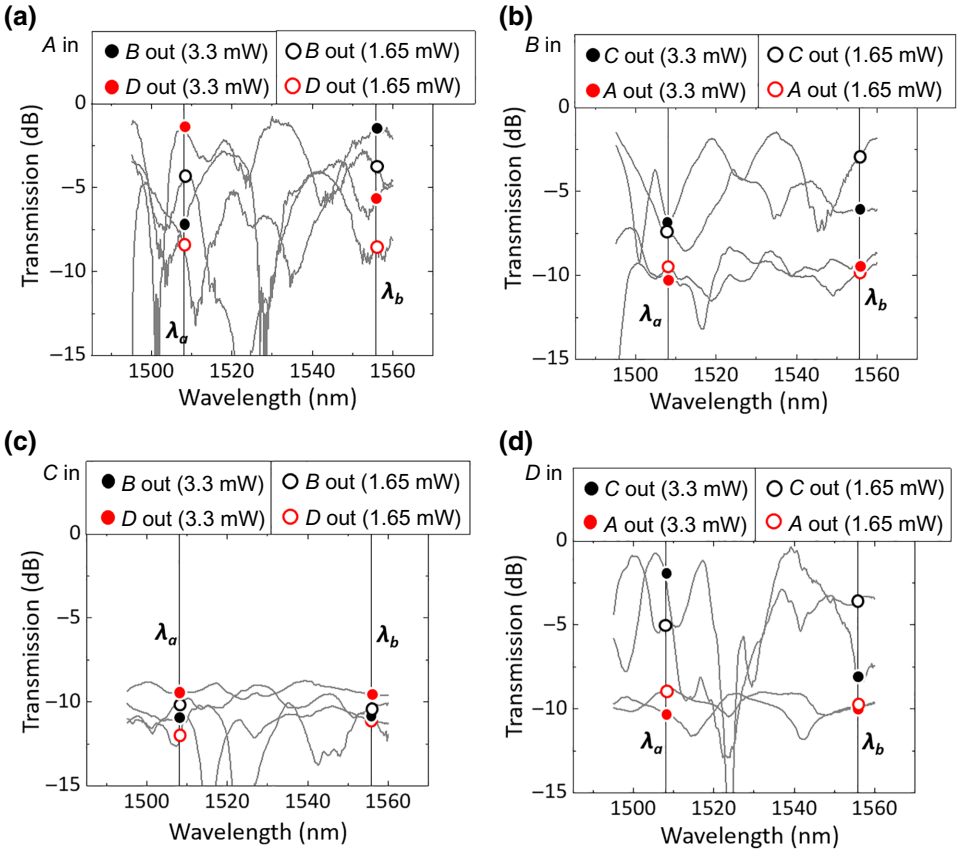

FIG. 4. Measured transmitted spectra with ports (a) *A*, (b) *B*, (c) *C*, and (d) *D* as the input port, respectively. The filled and empty circles mark the output intensities at the lower (Pin = 1.65 mW) and high input power levels (Pin = 3.3 mW), respectively. The relative distance between the circles visualizes the main output port.

the same peak as the single microring around λ_a and λ_b. It is shown in the spectra that, when the signal intensity changes (from the curves with hollow dots to those with solid dots), the resonance at around λ_a shifts, while that around λ_b does not. This fits well with our previous design.

(2) For *A*-*D* in (a) and *B*-*C* in (b), at the resonances, more energy goes through *A*-*B* and *D*-*C*, so there are valleys around λ_a and λ_b. The valleys also show the same shift.

(3) For *B*-*A* in (b), *C*-*B*, *C*-*D* in (c), and *D*-*A* in (d), the signal is blocked by the photonic crystal junction, so the output intensities are relatively low.

V. CONCLUSION

In summary, we design and fabricate a mode-selective router by means of a hybrid microring resonator operating at the anti-$\mathcal{PT}$ point. The anti-$\mathcal{PT}$-symmetry design is achieved by periodic subwavelength nonlinear material cladding around the perimeter of the microring resonator. The anti-$\mathcal{PT}$-symmetry design exhibits distinguished optical nonlinear switching power between adjacent modes. The device architecture provides an additional degree of freedom for optical signal processing in microring-resonator-based modulators and switches. The mode-selective switch can be integrated with other components for a multiroute router module, such as a mode-selective router. This work leads the way to the processing of large amounts of data in an integrated nanophotonic chip.

ACKNOWLEDGMENTS

This work was supported by the National Key Research and Development Program of China under Grants No. 2018YFB2200403 and No. 2018YFA0704404, by the National Natural Science Foundation of China under Grants No. 61775003, No. 11734001, No. 91950204, No. 11527901, and No. 91850111, and by the Beijing Municipal Science and Technology Commission under Grant No. Z191100007219001. T.G. is supported by the Air Force Office of Scientific Research (AFOSR) Grant No. FA9550-18-1-0300. F.F.W. is partially supported by NASA ECF Grant No. 80NSSC17K0526.

F. F. Wang and X. X. Niu contributed equally to this work.

[1] V. R. Almeida, C. A. Barrios, R. R. Panepucci, and M. Lipson, All-optical control of light on a silicon chip, Nature **431**, 1081 (2004).

[2] L. Luo, N. Ophir, C. Chen, L. H. Gabrielli, C. B. Poitras, K. Bergmen, and M. Lipson, Wdm-compatible mode-division multiplexing on a silicon chip, Nat. Commun. **5**, 3069 (2014).

[3] B. Stern, X. Zhu, C. P. Chen, L. D. Tzuang, J. Cardenas, K. Bergman, and M. Lipson, On-chip mode-division multiplexing switch, Optica **2**, 530 (2015).

[4] T. Hu, H. Qiu, P. Yu, C. Qiu, W. Wang, X. Jiang, M. Yang, and J. Yang, Wavelength-selective 4×4 nonblocking silicon optical router for networks-on-chip, Opt. Lett. **36**, 4710 (2011).

[5] D. Kleckner, W. T. M. Irvine, S. S. R. Oemrawsingh, and D. Bouwmeester, Diffraction-limited high-finesse optical cavities, Phys. Rev. A **81**, 043814 (2010).

[6] D. K. Gramotnev and S. I. Bozhevolnyi, Plasmonics beyond the diffraction limit, Nat. Photonics **4**, 83 (2010).

[7] W. Heni, Y. Kutuvantavida, C. Haffner, H. Zwickel, C. Kieninger, S. Wolf, M. Lauermann, Y. Fedoryshyn, A. F. Tillack, L. E. Johnson, D. L. Elder, B. H. Robinson, W. Freude, C. Koos, J. Leuthold, and L. R. Dalton, Silicon-organic and plasmonic-organic hybrid photonics, ACS Photonics **4**, 1576 (2017).

[8] J. A. Schuller, E. S. Barnard, W. Cai, Y. C. Jun, J. S. White, and M. L. Brongersma, Plasmonics for extreme light concentration and manipulation, Nat. Mater. **9**, 193 (2010).

[9] J. A. Scholl, A. García-Etxarri, A. L. Koh, and J. A. Dionne, Observation of quantum tunneling between two plasmonic nanoparticles, Nano Lett. **13**, 564 (2013).

[10] K. J. Savage, M. M. Hawkeye, R. Esteban, A. G. Borisov, J. Aizpurua, and J. J. Baumberg, Revealing the quantum regime in tunnelling plasmonics, Nature **491**, 574 (2012).

[11] J. Wang, Z. Sheng, L. Li, A. Pang, A. Wu, W. Li, X. Wang, S. Zou, M. Qi, and F. Gan, Low-loss and low-crosstalk 8×8 silicon nanowire AWG routers fabricated with CMOS technology, Opt. Express **22**, 9395 (2014).

[12] C. Koechlin, P. Bouchon, F. Pardo, J. Jaeck, X. Lafosse, J.-L. Pelouard, and R. Haïdar, Total routing and absorption of photons in dual color plasmonic antennas, Appl. Phys. Lett. **99**, 241104 (2011).

[13] Y. Fang, Z. Li, Y. Huang, S. Zhang, P. Nordlander, N. J. Halas, and H. Xu, Branched silver nanowires as controllable plasmon routers, Nano Lett. **10**, 1950 (2010).

[14] P. Fan, C. Colombo, K. C. Y. Huang, P. Krogstrup, J. Nygård, A. F. i Morral, and M. L. Brongersma, An electrically-driven gaas nanowire surface plasmon source, Nano Lett. **12**, 4943 (2012).

[15] H. Flayac and I. G. Savenko, An exciton-polariton mediated all-optical router, Appl. Phys. Lett. **103**, 201105 (2015).

[16] F. Marsault, H. S. Nguyen, D. Tanese, A. Lemaître, E. Galopin, I. Sagnes, A. Amo, and J. Bloch, Realization of an all optical exciton-polariton router, Appl. Phys. Lett. **107**, 201115 (2015).

[17] P. Miao, Z. Zhang, J. Sun, W. Walasik, S. Longhi, N. Litchinitser, and L. Feng, Orbital angular momentum microlaser, Science **353**, 464 (2016).

[18] Z. Wong, Y. Xu, J. Kim, K. O'Brien, Y. Wang, L. Feng, and X. Zhang, Lasing and anti-lasing in a single cavity, Nat. Photonics **10**, 796 (2016).

[19] H. Hodaei, M. Miri, M. Heinrich, D. Christodoulides, and M. Khajavikhan, Parity-time-symmetric microring lasers, Laser Photonics Rev. **346**, 975 (2014).

[20] M. Miri, P. LiKamW, and D. Christodoulides, Phase matching for large-scale frequency upconversion in plasma: Erratum, Opt. Lett. **37**, 764 (2012).

[21] C. Rüter, K. Makris, R. El-Ganainy, D. Christodoulides, M. Segev, and D. Kip, Parity-time-symmetric whispering-gallery microcavities, Nat. Phys. **6**, 192 (2010).

[22] A. Guo, G. J. Salamo, D. Duchesne, R. Morandotti, M. Volatier-Ravat, V. Aimez, G. A. Siviloglou, and D. N. Christodoulides, Observation of $\mathcal{PT}$-Symmetry Breaking in Complex Optical Potentials, Phys. Rev. Lett. **103**, 093902 (2009).

[23] B. Peng, S. Ozdemir, F. Lei, F. Monifi, M. Gianfreda, G. Long, S. Fan, F. Nori, C. Bender, and L. Yang, Parity-time-symmetric whispering-gallery microcavities, Nat. Phys. **10**, 394 (2014).

[24] A. Regensburger, C. Bersch, M. Miri, G. Onishchukov, D. Christodoulides, and U. Peschel, Parity-time synthetic photonic lattices, Nature **488**, 167 (2012).

[25] Z. Lin, H. Ramezani, T. Eichelkraut, T. Kottos, H. Cao, and D. N. Christodoulides, Unidirectional Invisibility Induced by $\mathcal{PT}$-Symmetric Periodic Structures, Phys. Rev. Lett. **106**, 213901 (2011).

[26] L. Chang, X. Jiang, S. Hua, C. Yang, J. Wen, L. Jiang, G. Li, G. Wang, and M. Xiao, Parity-time symmetry and variable optical isolation in active-passive-coupled microresonators, Nat. Photonics **8**, 524 (2014).

[27] Z. Luo, Y. Huang, M. Zhong, Y. Li, J. Wu, B. Xu, H. Xu, Z. Cai, J. Peng, and J. Weng, 1-, 1.5-, and 2-μm fiber lasers q-switched by a broadband few-layer MoS_2 saturable absorber, J. Lightwave Technol. **32**, 4679 (2014).

[28] F. Wang, X. Hu, H. Song, C. Li, H. Yang, and Q. Gong, Ultralow-power all-optical logic data distributor based on resonant excitation enhanced nonlinearity by upconversion radiative transfer, Adv. Opt. Mater. **5**, 1700360 (2017).

[29] See the Supplemental Material at http://link.aps.org/supplemental/10.1103/PhysRevApplied.14.044050 for the details (a detailed comparison with previous works in Sec. 1, the field distribution details in Sec. 2, how the design parameters influence the nonlinear tuning in Sec. 3, details of the heterojunction in Sec. 4, and details of the fabrication and measurement methods in Sec. 5).

[30] T. V. Menshchikova, M. M. Otrokov, S. S. Tsirkin, D. A. Samorokov, V. V. Bebneva, A. Ernst, V. M. Kuznetsov, and E. V. Chulkov, Band structure engineering in topological insulator based heterostructures, Nano. Lett. **13**, 6064 (2013).

[31] S. Cho, N. P. Butch, J. Paglione, and M. S. Fuhrer, Insulating behavior in ultrathin bismuth selenide field effect transistors, Nano. Lett. **11**, 1925 (2011).

[32] S. Lu, C. Zhao, Y. Zou, S. Chen, Y. Chen, Y. Li, H. Zhang, S. Wen, and D. Tang, Third order nonlinear optical property of Bi_2Se_3, Opt. Express **21**, 2072 (2013).

[33] H. Lee, T. Kananen, A. Soman, and T. Gu, Influence of surface roughness on microring-based phase shifters, IEEE Photonics Tech. Lett. **31**, 813 (2019).

[34] L. Feng, Z. Wong, R. Ma, Y. Wang, and X. Zhang, Single-mode laser by parity-time symmetry breaking, Science **346**, 972 (2014).

[35] T. Gu, M. Yu, D.-L. Kwong, and C. W. Wong, Molecular-absorption-induced thermal bistability in PECVD silicon nitride microring resonators, Opt. Express **22**, 18412 (2014).

[36] R. Boyd, *Nonlinear Optics* (Academic Press, Burlington, 2008).

[37] N. Sherwood-Droz, H. Wang, L. Chen, B. Lee, A. Biberman, K. Bergman, and M. Lipson, Optical 4×4 hitless silicon router for optical networks-on-chip (NOC), Opt. Express **16**, 15915 (2008).

[38] C. Wang, X. Zhong, and Z. Li, Linear and passive silicon optical isolator, Sci. Rep.-UK **2**, 674 (2012).

[39] C. Lu, X. Hu, H. Yang, and Q. Gong, Ultrahigh-contrast and wideband nanoscale photonic crystal all-optical diode, Opt. Lett. **36**, 4668 (2011).

[40] Y. Fu, X. Hu, C. Lu, S. Yue, H. Yang, and Q. Gong, All-optical logic gates based on nanoscale plasmonic slot waveguides, Nano Lett. **12**, 5784 (2012).

[41] Y. Zhang, Y. He, Q. M. Zhu, X. H. Jiang, X. H. Guo, C. Y. Qiu, and Y. K. Su, On-chip silicon polarization and mode handling devices, Front. Optoelectron. **11**, 77 (2018).

[42] S. Kaushal, R. Cheng, M. Ma, A. Mistry, M. Burla, L. Chrostowski, and J. Azaña, Optical signal processing based on silicon photonics waveguide Bragg gratings: Review, Front. Optoelectron. **11**, 163 (2018).